



# Synthesis and characterization of mixed ternary transition metal ferrite nanoparticles comprising cobalt, copper and binary cobalt–copper for high-performance supercapacitor applications

Sherief A. Al Kiey<sup>1,2</sup> · Rania Ramadan<sup>3</sup> · Mai M. El-Masry<sup>4</sup>

Received: 25 February 2022 / Accepted: 9 April 2022 / Published online: 9 May 2022  
© The Author(s) 2022

## Abstract

Metal ferrites have outstanding electrochemical characteristics owing to the numerous oxidation states of the metal ions, making them promising materials for addressing both sustainable energy conversion and storage and growing environmental issues. Therefore, three nanocrystallites transition metal ferrites,  $\text{CoFe}_2\text{O}_4$ ,  $\text{CuFe}_2\text{O}_4$  and  $\text{Co/CuFe}_2\text{O}_4$ , were synthesized using citrate precursors and used as electrode materials for supercapacitor applications. Mixed transition metal ferrite nanoparticles were characterized by Fourier transform infrared (FT-IR), scanning electron microscope (SEM) complemented with energy-dispersive spectroscopy (EDX), transmission electron microscopy (TEM), Raman spectroscopy and thermal analysis (TGA). The findings illustrated the formation of a single-phase spinel ferrite as proved from XRD data. In addition, the particle shape and particle size obtained from TEM analysis revealed that the as-synthesised nanomaterial exhibited spherical shape with a size ranging from 30 to 50 nm. The result demonstrated that while using a three-electrode configuration, the electrochemical performance of the ferrite nanoparticles achieved a remarkable maximum specific capacitance of  $893 \text{ Fg}^{-1}$  at a scan rate of  $5 \text{ mV s}^{-1}$ . At a current density of  $1 \text{ Ag}^{-1}$ , Co–Cu ferrite exhibited outstanding cycling stability for 3000 cycles with 90% capacity retention. Based on the aforementioned data, it can be considered that the remarkable electrochemical performance of the Co–Cu ferrite nanocomposites can be considered as promising materials to be used for supercapacitor electrodes.

**Keywords** Ferrite · Magnetic properties · Dielectric properties · Supercapacitor · EIS

## 1 Introduction

Fossil fuels, which provide 80% of the world's oil, are rapidly depleting [1, 2]. Several developed and developing countries are looking for renewable energy sources to meet the energy demand and reduce greenhouse gas emissions. Solar, wind, tidal, and geothermal energy are the most

common and widely pursued sources of renewable, sustainable energy [3].

Batteries and supercapacitors are electrochemical energy storage devices with unique energy and power densities, cycling stability, and charging–discharging speeds. Supercapacitors have already begun to replace batteries in a number of applications where the energy consumption is low, but the power demand is strong, such as electric power tools, phone chargers, and portable vacuum cleaners. Their key benefits are that, unlike batteries, they can be completely charged in minutes rather than hours, and they have a high power capacity [4]. Unfortunately, the lower energy density of supercapacitors in comparison to batteries is a significant limiting factor for their use in place of batteries [5–8]. As a result, it is critical to investigate new materials for supercapacitor electrodes that meet the demands of industrial energy firms for high-power density and long longevity [9]. Supercapacitors can be classified into two types of energy storage mechanisms: electrochemical double layer capacitors with carbon electrodes [10] and pseudo-capacitors with transition

✉ Sherief A. Al Kiey  
sheriefalkiey@yahoo.com

<sup>1</sup> Electrochemistry and Corrosion Laboratory, National Research Centre, Dokki 12622, Cairo, Egypt

<sup>2</sup> Material Engineering Lab, National Research Centre, Dokki 12622, Cairo, Egypt

<sup>3</sup> Materials Science Laboratory, Physics Department, Faculty of Science, Cairo University, Giza, Egypt

<sup>4</sup> Basic Science Department, Higher Engineering Institute, Thebes Academy, Cairo, Egypt

metal oxides or conducting polymer electrodes [11]. Transition metal oxides, such as NiO, Co<sub>3</sub>O<sub>4</sub>, Fe<sub>2</sub>O<sub>3</sub>, MnO<sub>2</sub>, V<sub>2</sub>O<sub>5</sub>, and spinel oxides utilize fast and reversible faradaic redox processes (pseudo-capacitance) involving ions and electrons in their charge storage mechanism [12, 13].

Ferrites are one of the most important materials for a variety of applications, including ceramics, pigments, electronics, microwave absorbents, supercapacitors, and solid state batteries [14–16]. The size, shape, and composition of the particles, which are regulated by the preparation process, determine the properties and applications of these materials [17–20]. Recent reports have successfully reported the synthesis of ferrite nanostructures with tunable size and morphology, including hollow spheres [21], nanocrystals [22] and nanorods/nanowires [23], using a variety of synthetic approaches [24–27]. Several investigations on ferrite nanomaterials, including nickel ferrite, cobalt ferrite, manganese ferrite, and copper ferrite, have been conducted [28–35]. It is assumed that ferrite oxides (MFe<sub>2</sub>O<sub>4</sub>) will have greater redox activities, including involvement from both M and Fe ions, unlike monometallic oxides. Designing innovative ferrite-based hybrids is a promising way to improve performance. Mixed ferrites are ferrite spinels that are composed of a mixture of two divalent metal ions, with varying ratios. The surface properties of ferros spinels are considerably affected by the cation distribution of mixed ferrite, making them catalytically active. Nanocrystallites can accelerate chemical reactions because of their small size and huge number of cations for co-ordination sites, and they are becoming more popular as reactive nanocrystallites. Kumbhar et al. [33] studied the synthesis of cobalt ferrite nanoflakes, by a simple chemical route. The electrochemical characteristics of ferrite thin films were studied and achieved a maximum capacitance of 366 F g<sup>-1</sup> at 5 mV s<sup>-1</sup>. Pawar et al. [36] used the sol–gel process to synthesize Co ferrite nanoparticles for use in supercapacitors achieving 15 Fg<sup>-1</sup> at a current density of 0.6 Ag<sup>-1</sup>. The poor electrical conductivity of CoFe<sub>2</sub>O<sub>4</sub> nanoparticles could explain the lower capacitance value. Deng et al. [37] investigated the electrochemical characteristics of CoFe<sub>2</sub>O<sub>4</sub> nanoparticles. It should be emphasized, however, that pure CoFe<sub>2</sub>O<sub>4</sub> is not conductive enough to produce satisfactory results.

Therefore, designing innovative CoFe<sub>2</sub>O<sub>4</sub>-based hybrids are a promising way to boost performance. Due to their high theoretical specific capacitance, well-defined redox behavior, low cost, and environmental friendliness, spinel–copper composites are also a promising potential for supercapacitor applications. As a consequence, it is interesting to investigate the applicability of mixed ternary transition metal ferrites, ABFe<sub>2</sub>O<sub>4</sub>, nanocomposites produced of copper ferrite, cobalt ferrite, and cobalt-copper ferrite in the challenging field of supercapacitors as potential electrode materials with high capacitance values. Cu ferrite, Co ferrite, and Cu–Co

ferrite are other attractive materials for supercapacitors, because they are affordable and non-toxic.

In the present work, we have synthesized Co ferrite, Cu ferrite and binary Cu–Co ferrite nanoparticles via a citrate combustion method. Combustion method is an effective, low-cost method to synthesize different oxide materials. The structure and morphology were characterized using XRD, FE-SEM, HR-TEM, and FTIR and the magnetic behavior was studied using VSM. Finally, the electrochemical performance measurements of the supercapacitors in a three-electrode system were performed by cyclic voltammetry, galvanostatic charge–discharge and impedance spectroscopy at room temperature in an alkaline medium (1 M KOH). A promising electrochemical performance of Co–Cu mixed ferrite nanoparticles was achieved, with a maximum specific capacitance of 893 Fg<sup>-1</sup> at a scan rate of 5 mV s<sup>-1</sup>. At a current density of 1 Ag<sup>-1</sup>, Co–Cu ferrite exhibited outstanding cycling stability for 3000 cycles with 90% capacity retention.

## 2 Experimental work

### 2.1 Materials

All the chemicals used in this study were of analytical grade and were used as received without further purification. Cobalt nitrate (Co(NO<sub>3</sub>)<sub>2</sub>, 98%), copper nitrate (Cu(NO<sub>3</sub>)<sub>2</sub>, 98%), iron nitrate (Fe(NO<sub>3</sub>)<sub>3</sub>, 98%) and citric acid were used as fuel for this method (Alfa Aeser). Polyvinylidene fluoride PVDF, carbon black and *N*-methylpyrrolidone (NMP) were the analytical reagents purchased from Alfa Aeser. Nickel foam was supplied by the Shanghai Hongxiang Plant.

### 2.2 Synthesis of ferrite nanoparticles

The citrate combustion method was used to synthesize Co ferrite, Cu ferrite, and Cu–Co ferrite nanoparticles. Co ferrite was synthesized by adding 10 mmol of cobalt nitrate and iron nitrate each to a 50 mL aqueous solution of citric acid (10 mmol) in a 1000 mL beaker. At room temperature, the mixture was rapidly stirred for 6 h. The pH of the solution was then raised to 7.0. To create a fine powder, the temperature was increased to 250 °C until all fumes were ended. After cooling in air, the final powder was ground at a rate of 4 °C/min, and the finished powder was calcined for 4 h at 800 °C. The previous method was repeated to prepare Cu ferrite, where cobalt nitrate (5 mmol), copper nitrate (5 mmol), and iron nitrate (10 mmol) were added to a 50 mL aqueous solution of citric acid (10 mmol) to prepare Co–Cu ferrite nanoparticles.

## 2.3 Physical characterization

The structural characterization of the samples was performed by powder X-ray diffraction (XRD) using Proker D8 advance X-ray diffractometer with CuK $\alpha$  radiation ( $\lambda = 1.5418 \text{ \AA}$ ). Field emission scanning electron microscopy (FESEM) Sigma 300VP operated at 10 kV. Gwyddion software Version 2.32 was used to analyze the surface topological roughness features of ferrite nanoparticles to convert the 2D FE-SEM image to a 3D image [38, 39]. High-resolution transmission electron microscope (HRTEM) JEM-ARM300F operating at 200 kV was used. The infrared (IR) spectra for all samples were recorded by an FTIR instrument (Perkin Elmer) in the range of 4000–400  $\text{cm}^{-1}$ . The structure of the materials was characterized using Raman spectroscopy with an Nd:YAG laser operating at a wavelength of 532 nm at room temperature. Vibrating sample magnetometer (VSM) Lakeshore 7410S was used. Using the SDT Q600 USA thermal analyzer, thermogravimetric analysis (TGA) of composites was carried out in the nitrogen atmosphere with a heating rate of 10  $^{\circ}\text{C}/\text{min}$ . The Quantachrome Nova-1000 method was used to analyze the sample's  $\text{N}_2$  adsorption and desorption isotherms at 77 K temperature.

An LCR Hi Tester evaluated the dielectric of the prepared synthesized ferrite nanoparticles (HIOKI, 3532–50).

The real part  $\epsilon'$  and the imaginary part  $\epsilon''$  of the dielectric function of the samples were estimated from the measured capacitance ( $C_p$ ), by means of the equations [40]:

$$\epsilon' = \frac{C_p d}{\epsilon_o A}, \quad (1)$$

$$\epsilon'' = \epsilon' \tan \delta, \quad (2)$$

where  $d$  is the thickness of the sample (m),  $\epsilon_o$  is the permittivity of free space ( $8.85 \times 10^{-12}$ ),  $A$  is the sample effective surface area ( $\text{m}^2$ ) and  $D$  is the loss tangent ( $\tan \delta$ ), obtained directly from the instrument.

## 2.4 Electrode preparation and electrochemical measurements

The active material mass of the prepared samples of (Co ferrite, Cu ferrite, Co–Cu ferrite) powder (80 wt%) was mixed with carbon black (10 wt%) as a conducting agent and polyvinylidene fluoride (PVDF) dissolved in *N*-methyl-2-pyrrolidone (NMP) (10 wt%) as a binder. To remove the nickel oxide top surface layer, the nickel foam was pretreated and washed in HCl solution for 15 min and then rinsed in deionized water (DI) water and ethanol. The resulting paste was casted onto nickel foam (current collector). In an oven, the coated nickel foam was dried overnight at 60  $^{\circ}\text{C}$ . The

electrochemical measurements were carried out using an electrochemical station (Volta lab 40, PGZ 301, France) in a three-electrode system with a coated active material on a nickel foam as the working electrode, Ag/AgCl as the reference electrode, and platinum strip as the counter electrode. 1 M KOH aqueous solution was employed as the aqueous electrolyte for cyclic voltammetry (CV), galvanostatic charge–discharge (GCD), and electrochemical impedance (EIS). CV characterization was carried out in the 0–0.5 V potential range at various scan rates (5–200 mV/s). GCD measurements were made at varying current densities (1–10 A/g). EIS measurements were carried out in the frequency range of 100 kHz–0.1 Hz at open circuit potential with a 10 mV sinusoidal perturbation amplitude. From CV and GCD measurements, the specific capacitance ( $C_{sp}$ , F/g) was calculated using the following equation [41, 42]:

$$C_{sp} = \frac{i}{mv} = \frac{\int_{v_1}^{v_2} i(V) dV}{mv \Delta V}, \quad (3)$$

where the specific capacitance ( $C_{sp}$ ) values of the electrodes were also evaluated based on cyclic voltammetric (CV) data,  $m$  equals the active material mass (g),  $v$  is the scan rate (mV/s), and  $i$  (V) is the current response during the potential scan.

Also, the  $C_{sp}$  values can be calculated based on the charge/discharge data using the following equation [43]:

$$C_{sp} = \frac{I \Delta t}{m \Delta V}, \quad (4)$$

where  $C_{sp}$  is the capacitance of the material,  $I$  is the applied current, and  $dV/dt$  is the slope of the discharging GCD curve.

## 3 Results and discussion

### 3.1 Physicochemical characterization

The crystal structure of the synthesized nanoparticles was confirmed by X-ray diffraction. The X-ray diffraction patterns of the synthesized Co ferrite, Cu ferrite, and Co–Cu ferrite nanoparticles are shown in Fig. 1. The figure confirms the formation of single-phase compounds, where the XRD pattern of the investigated samples is compatible with the reference ICDD cards [01-082-8784] with tetragonal structure, [04-005-7078] with cubic structure and [00-065-0376] with a cubic structure for  $\text{CuFe}_2\text{O}_4$ ,  $\text{CoFe}_2\text{O}_4$  and  $\text{Cu–CoFe}_2\text{O}_4$ , respectively. Few peaks appeared corresponding to the hematite according to the ICDD card [04-015-9572]. There were no peaks from other phases or impurities, indicating that the ferrite nanoparticles were very pure. The crystalline nature of the prepared samples is described by the intensity and sharpness of the peaks.

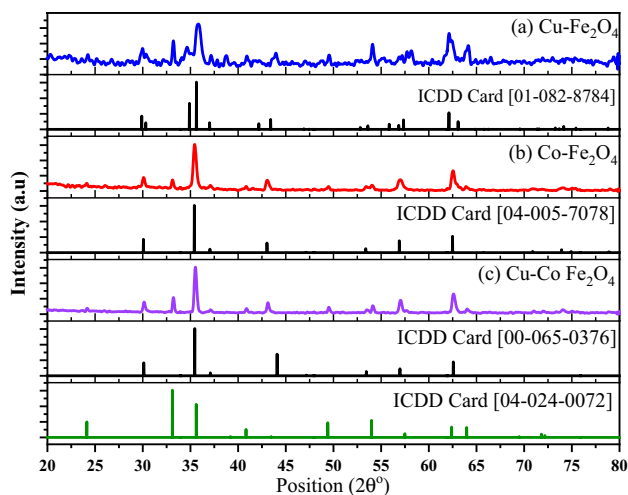


Fig. 1 XRD spectrum of **a** Cu ferrite, **b** Co ferrite, **c** Co–Cu ferrite

The crystallite size *D* was calculated according to the Scherrer equation [44, 45]:

$$D = \frac{0.9\lambda}{\beta \cos\theta}, \tag{5}$$

where  $\lambda$  is the wavelength of the radiation,  $\theta$  is the diffraction angle and  $\beta$  is the full width at half maximum (FWHM) of the diffraction peak.

The crystallite size of the CoFe<sub>2</sub>O<sub>4</sub>, CuFe<sub>2</sub>O<sub>4</sub>, and Co–Cu Fe<sub>2</sub>O<sub>4</sub> nanoparticles was 20, 24 and 22 nm and the lattice constant was 8.4, 5.9 and 8.42, respectively. CuFe<sub>2</sub>O<sub>4</sub> and Co–Cu Fe<sub>2</sub>O<sub>4</sub> have larger crystallite sizes as well as the unit cell parameters of CuFe<sub>2</sub>O<sub>4</sub> and Co–Cu Fe<sub>2</sub>O<sub>4</sub> increased, since copper has an ionic radius greater than that of cobalt.

The surface morphology and microstructure of ferrite nanoparticles were studied by field emission scanning electron microscopy FESEM. The FESEM images of ferrite grains are shown in Fig. 2a, Cu ferrite (Fig. 2c), and Co–Cu ferrite (Fig. 2e), respectively, while HRTEM images of the ferrite particles are shown in Fig. 4 (Co ferrite (Fig. 4a), Cu ferrite (Fig. 4b), and Co–Cu ferrite (Fig. 4c), respectively). According to FESEM, there is agglomeration and the crystals are spherical with irregular shapes and their size ranges from 60 to 220 nm. The EDX investigation (Fig. 2b, d, f) revealed peaks for Co, Fe, and O supporting the synthesis of Co ferrite, peaks for Cu, Fe and O supporting the synthesis of Cu ferrite, and peaks for Co, Cu, Fe and O supporting the synthesis of Co–Cu ferrite.

Because of the small particle sizes, the process of agglomeration can be explained. These sample agglomeration phenomena can be explained by their small particle

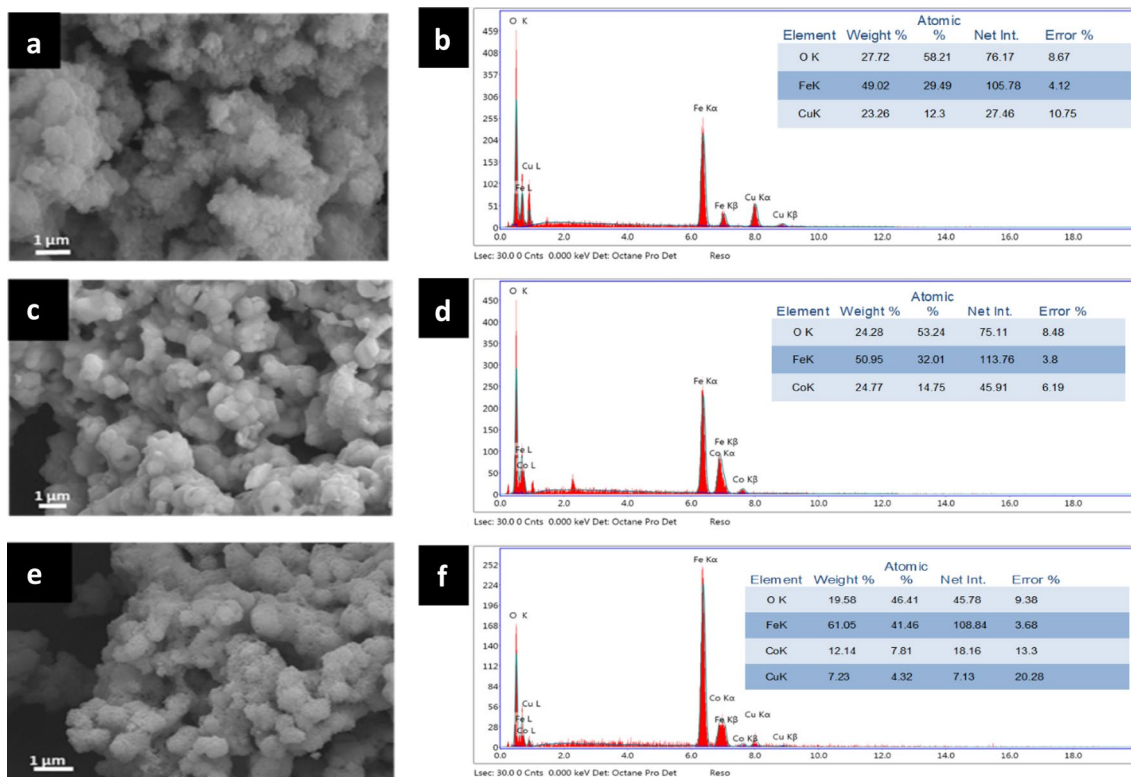
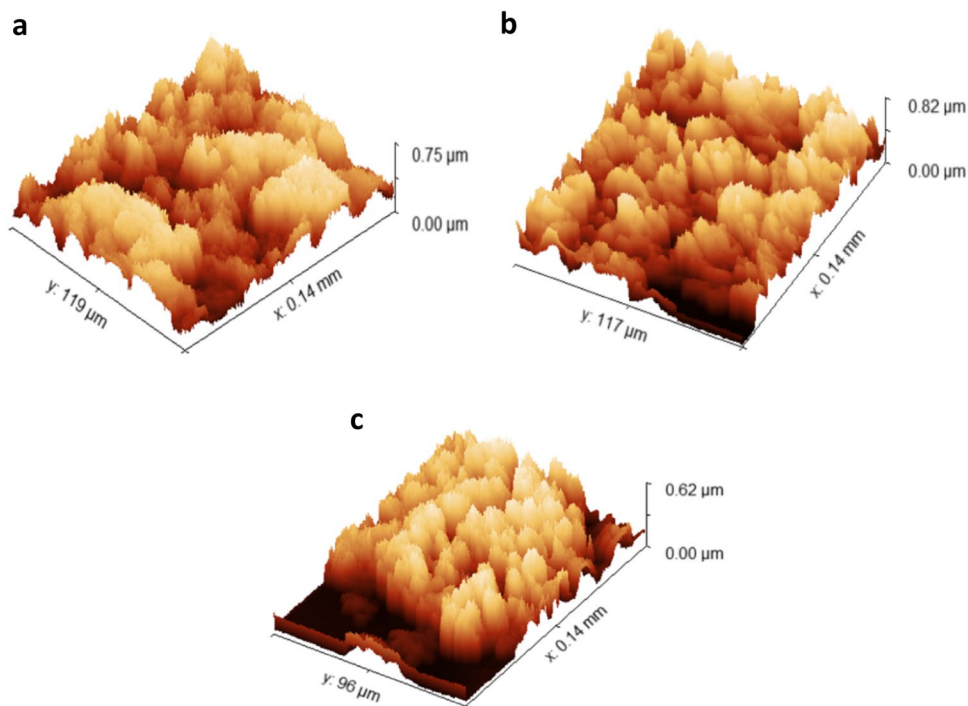
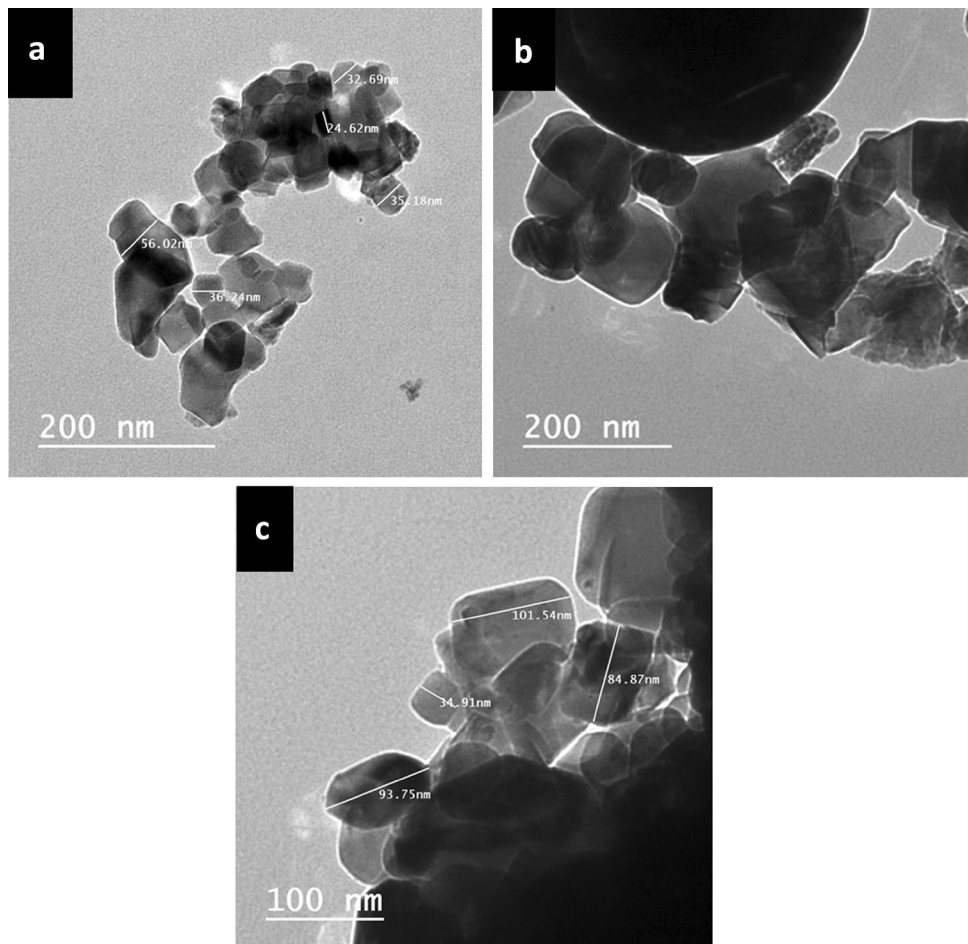


Fig. 2 FESEM–EDX micrographs of **a, b** Co ferrite, **c, d** Cu ferrite, and **e, f** Co–Cu ferrite

**Fig. 3** Surface roughness behavior of ferrite nanoparticles. **a** Cu ferrite, **b** Co ferrite and **c** Co–Cu ferrite



**Fig. 4** HRTEM micrographs of **a** Co ferrite, **b** Cu ferrite and **c** Co–Cu ferrite



sizes and lack of steric hindrance, both of which make it easier for particles to come together and form agglomerates.

Figure 3 shows three-dimensional (3D) micrographs of representative ferrite nanoparticles. Co–Cu ferrite exhibits higher roughness and porosity than Co ferrite and Cu ferrite, according to the roughness micrograph analysis. The larger copper ions' radius causes inhomogeneity and higher pore sizes which increase the roughness and porosity [46]. As a result, Co–Cu ferrite has a greater surface-to-volume ratio, making it suited for supercapacitor applications because it provides a simple path for ion migration at the electrode–electrolyte interface. The roughness values of 45, 13 and 8.5 nm are found on the surfaces of Co–Cu ferrite, Co ferrite, and Cu ferrite, respectively.

HRTEM micrographs of Co ferrite, Cu ferrite, and Cu–Co ferrite in Fig. 4a–c reveal a uniform distribution of polycrystalline nanoscale particles. Co ferrite, Cu ferrite, and Cu–Co ferrite nanoparticles are composed of standardized cubic crystals with average crystal sizes of 30.04 nm, 53.1 nm, and 43.7 nm, respectively.

FT-IR spectra of all Co ferrite, Cu ferrite and Co–Cu ferrite nanoparticles are shown in Fig. 5a. According to the geometrical structure in ferrite, the metal ions are located in two separate sublattices, namely tetrahedral (A-sites) and

octahedral (B-sites). The spectra reveal two major transmittance bands at 500 and 400  $\text{cm}^{-1}$ , which are reported to be due to the metal oxide stretching vibrations of the octahedral and tetrahedral sites in spinels, respectively [46, 47]. This helps to understand why a tetrahedral cluster's regular mode of vibration is higher than an octahedral cluster's. The FT-IR spectra also show a peak at  $\sim 1640 \text{ cm}^{-1}$  and a wide-ranging band peak at  $\sim 3440 \text{ cm}^{-1}$ , which are appointed to the O–H stretching modes and H–O–H bending vibration of free or absorbed water [48, 49]. The samples' spinel structure of ferrite nanoparticles was verified by the FTIR results, which were discovered by XRD results.

Raman spectroscopy is an effective technique for detecting numerous lattice phenomena that exhibit themselves as vibrational mode variations [50]. The structural characteristics of (Cu, Co, Co–Cu) ferrites were further revealed by recording the Raman spectra of ferrites, as shown in Fig. 5b. Spinel ferrite, in general, is a cubic spinel structure that belongs to the Oh7 space group (Fd-3 m). Tetrahedron and octahedron in the lattice are made up of oxygen anion ( $\text{O}^{2-}$ ), and metal ions occupy both the tetrahedral and octahedral sites. There are five Raman-active modes in the spinel group, ( $A_{1g} + E_g + 3T_{2g}$ ), which correlate with the mobility of O ions and ions at A-sites and B-sites [51, 52].

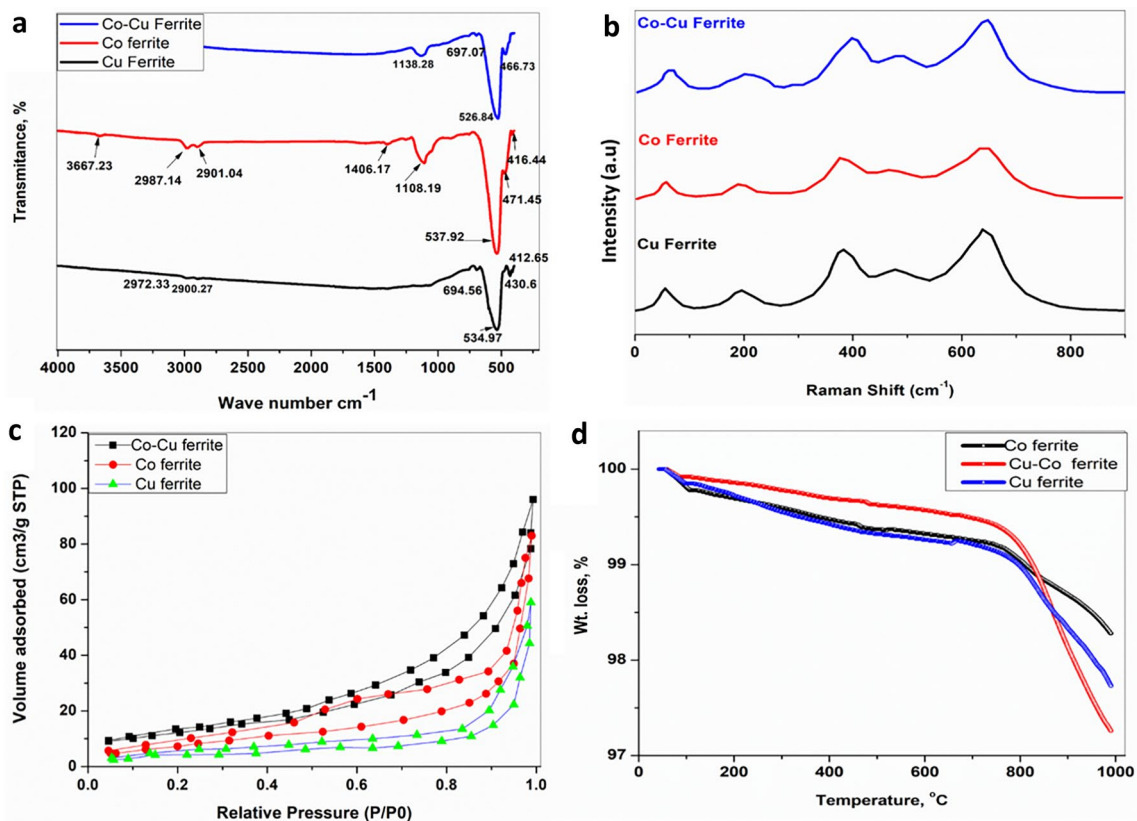


Fig. 5 **a** FT-IR spectra, **b** Raman spectra, **c**  $\text{N}_2$  adsorption–desorption, and **d** thermal gravimetric analysis (TGA) of ferrite nanoparticles

The  $A_{1g}$  corresponds to the oxygen anion symmetric stretching vibration, whereas  $E_g$  corresponds to the oxygen anion symmetric bending vibration, and  $T_{2g}$  corresponds to the asymmetric stretching vibration between oxygen anions and cations in the A-site and B-site [53]. All of the Raman peaks were attributed to the  $A_{1g}$ ,  $T_{2g}$ , and  $E_g$  modes, which represent the vibration of spinel structures, showing that pure (Cu, Co, Co–Cu) ferrite was achieved. The surface area is an extremely important property to consider when evaluating supercapacitor electrode materials. The  $N_2$  adsorption–desorption isotherms of the three investigated ferrite nanoparticles are shown in Fig. 5c. The BET method and the desorption isotherms of Barrett–Joyner–Halenda (BJH) plots are used to determine the specific surface area (SSA) utilizing the gas sorption analysis with  $N_2$  adsorption–desorption isotherms. The IUPAC classification system is used to classify adsorption/desorption isotherms. The isotherms of the evaluated magnetic nanomaterials samples were connected by means of H3 hysteresis loop on a type IV curve. This hysteresis loop is linked to capillary condensation in the mesopores, which occurs when the adsorption and desorption curves do not line up. BET analysis of type IV isotherms can be used to determine the actual surface area of ferrite nanoparticles. Co–Cu ferrite nanoparticles with a high surface area ( $98\text{ m}^2/\text{g}$ ) have a mesoporous nature that can increase and facilitate ion and electron diffusion and

transport at the electrolyte–electrode interface, resulting in improved electrochemical performance. From the data obtained from surface area, it can be concluded that Co–Cu ferrite nanoparticle has the highest surface area value, followed by Co ferrite ( $76\text{ m}^2/\text{g}$ ) and Cu ferrite ( $54\text{ m}^2/\text{g}$ ). To determine the material thermal stability, thermal gravimetric analysis was performed based on weight loss as a function of temperature. The TGA curves for the sample Co ferrite, Cu ferrite, and Co–Cu ferrite heated to  $1000\text{ }^\circ\text{C}$  at  $10\text{ }^\circ\text{C}/\text{min}$  in  $N_2$  atmosphere are shown in Fig. 5d. The thermal breakdown of as-prepared ferrite nanoparticles includes three steps. The evaporation of absorbed water and primary breakdown of the complex initially caused weight loss at temperatures between  $50$  and  $150\text{ }^\circ\text{C}$ . The second stage in TGA suggests that organic matter can decompose due to the precursor's components, chelating agents, and solvents, resulting in the creation of the oxide phase. The formation of spinel phase metal oxide is responsible for the final stage of weight loss at temperatures about  $800\text{ }^\circ\text{C}$ . This shows how pure ferrite is formed.

### 3.2 Dielectric properties

Figure 6 depicts the frequency dependence of the real part ( $\epsilon'$ ) and imaginary part ( $\epsilon''$ ) of the dielectric constant of as-synthesized ferrite nanoparticles. Figure 6 shows that the

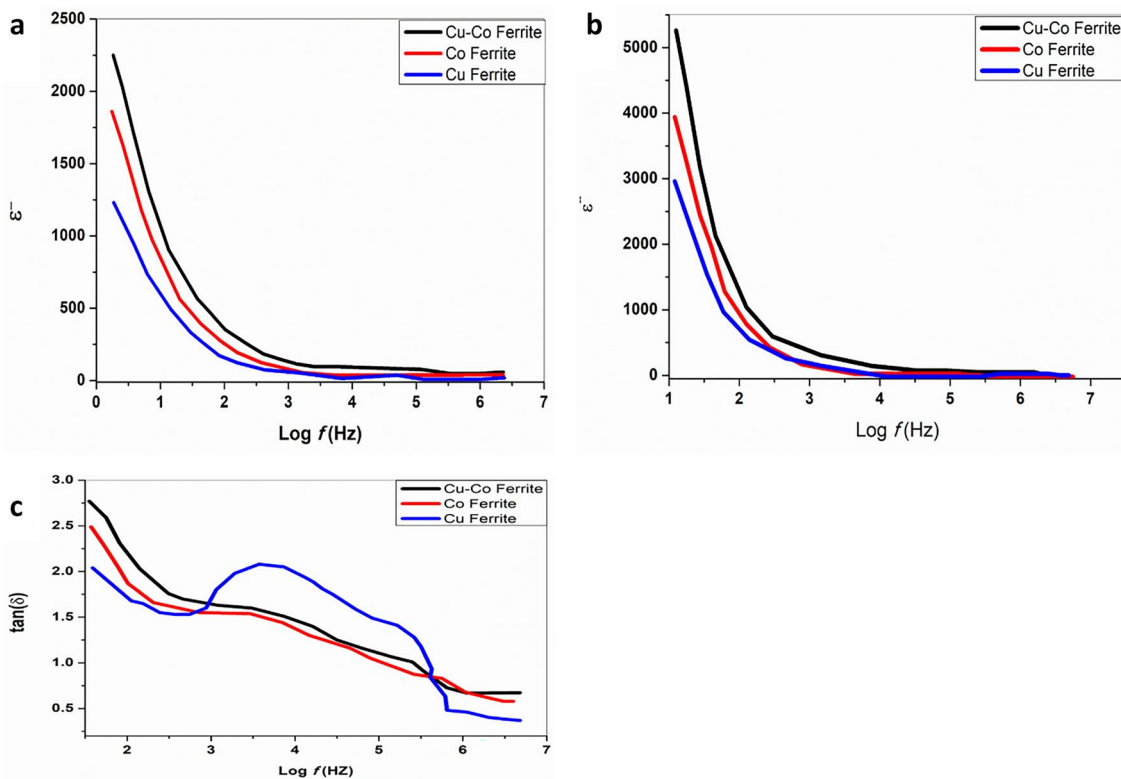


Fig. 6 Real, a  $\epsilon'$  and imaginary, b  $\epsilon''$  dielectric constant and c dielectric loss ( $\tan \delta$ ) as a function of frequency for ferrite nanoparticles

dielectric constant drops as the frequency increases. It drops swiftly from 1 to 100 Hz at lower frequencies, then slowly at higher frequencies. The contributions from ionic, space charge, and interfacial polarization are connected with the high value of dielectric constant at lower frequencies. The dielectric constant becomes frequency independent at higher frequencies, because electric dipoles cannot keep up with the quick changes in the applied electric field [54]. Koop's hypothesis [55], which posits the dielectric structure as an inhomogeneous medium of two layers of the Maxwell–Wagner type [56], can explain the drop in dielectric constant with frequency. As a result, the dielectric constant is large at low frequencies and drops as frequency increases [57]. The polarization of spinel ferrite occurs via a mechanism similar to that of conduction. Polarization in as-synthesized ferrite nanocomposite is caused by charge carriers hopping, and as a result, at low frequencies, charge carriers hitting grain boundaries pile up there due to the increased resistance, causing polarization. As the frequency of the applied ac electric field increases, the charge carriers are unable to follow the frequency of the applied ac electric field and polarization decreases [58].

Figure 6c depicts the variation of dielectric loss ( $\tan \delta$ ) with frequency for ferrite nanoparticles. Grain boundaries, impurities, and imperfections in the spinel ferrite crystal lattice cause dielectric loss in polycrystalline spinel ferrite, which is linked to a lag in polarization with respect to the applied ac electric field. When the hopping frequency of the charge carriers is equal to the frequency of the external a.c. electric field, the greatest electrical energy is transmitted to the oscillating ions, resulting in a peak in power loss [59], as shown in Fig. 6c. The requirement for the greatest dielectric loss in the material is  $\omega\tau = 1$ , where  $\omega = 2\pi f$ . The jumping probability per unit time ( $p$ ) is related to the relaxation time ( $\tau$ ) as  $\tau = 1/2p$ , or  $\omega_{\max} = 2p$  [60]. The conduction process in spinel ferrite happens with both n-type and p-type charge carriers. Between  $\text{Fe}^{2+}$  and  $\text{Fe}^{3+}$  ions, n-type charge transfer takes place, while between  $\text{Co}^{2+}$  and  $\text{Co}^{3+}$  ions and  $\text{Cu}^{1+}$  to  $\text{Cu}^{2+}$  p-type charge transfer takes place. When the rate of hopping approaches the frequency of the supplied ac electric field, the Debye relaxation process occurs.

### 3.3 Magnetic properties

The magnetic measurements provide information about the magnetic parameters such as saturated magnetic intensity ( $M_s$ ), residual magnetic intensity ( $M_r$ ), coercivity ( $H_c$ ) and squareness ratio. The  $M_s$  measurements were done in magnetic fields up to 10 T. In the absence of saturation,  $M_s$  was estimated by fitting the magnetization vs. field curve  $M(H)$ . Figure 7 shows a hysteresis loop diagram of  $\text{CoFe}_2\text{O}_4$ ,  $\text{CuFe}_2\text{O}_4$ , and  $\text{Co-CuFe}_2\text{O}_4$  nanoparticles. The as-saturated magnetic intensity ( $M_s$ ), residual magnetic

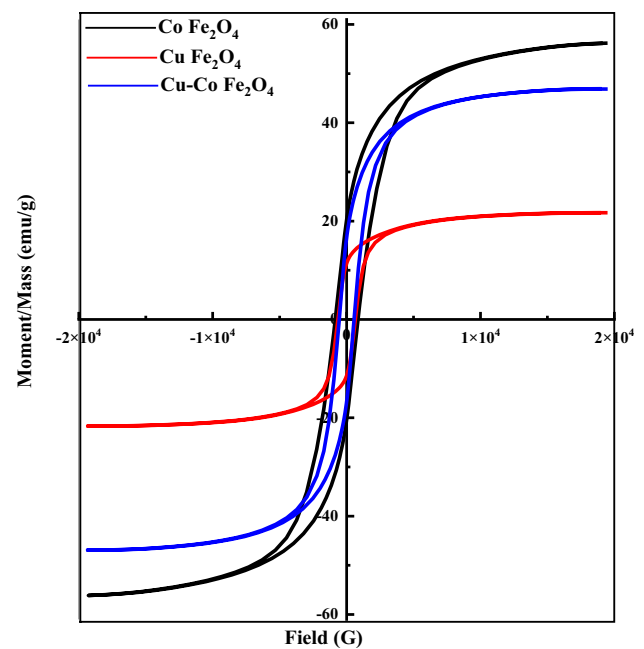


Fig. 7 VSM analysis of  $\text{CoFe}_2\text{O}_4$ ,  $\text{CuFe}_2\text{O}_4$ , and  $\text{Co-CuFe}_2\text{O}_4$

intensity ( $M_r$ ), coercivity ( $H_c$ ) and squareness ratio are shown in Table 1. The hysteresis loops of the prepared samples are of typical ‘S’ type, showing obvious ferrous magnetism. However, the magnetic strength of the samples varies with the different samples.

Among them, the saturated magnetic strength of  $\text{Co}$  ferrite has the greatest value of 56.19 emu/g. According to the geometrical arrangement of the oxygen nearest neighbors, the metal ions in ferrite are arranged in the two sublattices, tetrahedral (A-sites) and octahedral (B-sites). The saturation values are explained by the assumption that the A–B interaction favors anti-parallel coupling of the A-site and B-site groups and is strong enough to overcome any tendency for A–A or B–B couplings to disrupt the parallel alignment of all spins within the A-site or B-site groups separately [61]. For  $\text{Cu}$  ferrite nanoparticles, in the nanoscale the crystal structure is no longer a complete ‘normal’ spinel ferrite, and part of  $\text{Fe}^{3+}$  and  $\text{Cu}^{2+}$  exchange their positions, so that short-range interactions occur in the crystal, resulting in magnetism in the non-magnetic copper ferrite [62]. It is observed that  $M_s$ ,  $M_r$ ,  $H_c$  and squareness ratio of  $\text{Co}$  ferrite decrease with copper substitution [63]. It could be caused by a decrease in the magnetization of the B-site causing a decrease in the net magnetization. The replacement of  $\text{Co}^{2+}$  ions by  $\text{Cu}^{2+}$  ions leads to a reduction of the super-exchange interaction between the A and B sites. In other words, the copper contribution leads to a decrease in the  $H_c$  values which could be explained based on domain structure, critical diameter and the anisotropy of the crystal [64].

**Table 1** Magnetic parameters of as-synthesized ferrite nanoparticles

Magnetic parameters	Co ferrite	Cu ferrite	Co–Cu ferrite
Magnetic saturation (Ms) (emu/g)	56.168	21.696	46.912
Residual magnetic intensity (Mr) (emu/g)	20.267	11.411	16.681
Coercivity (Hc) (G)	851.1	649.55	555.07
Squareness ratio	0.36	0.525	0.355

### 3.4 Electrochemical characterization

CV and GCD measurements were used to investigate and analyze the electrochemical supercapacitive performance of the investigated ferrite nanoparticles. The CV curves of investigating ferrite nanoparticles are shown in Fig. 8 in 1 M KOH as the electrolyte at different scan rates in the potential range of 0.0–0.5 V vs. Ag/AgCl. Two peaks appear on the CV curves for the oxidation and reduction processes, respectively, at 0.38 V and 0.2 V, showing faradaic-type capacitive characteristics. As shown in Fig. 9, the maximum specific capacitance  $C_{sp}$  (893, 458 and 378 F/g for Co–Cu ferrite, Co ferrite and Cu ferrite, respectively) is achieved at 5 mV/s (the slowest scan rate), while  $C_{sp}$  is 255, 170 and

125 F/g at 200 mV/s for Co–Cu ferrite, Co ferrite and Cu ferrite, respectively. Furthermore, at high scan rates, the diffusion of electrolyte ions through the electrode, where faradaic reactions occur, is reduced [65, 66]. This behavior suggests that certain parts of the electrode surface are unavailable at high charging/discharging rates [67]. As a result, for electrochemical energy stored in the investigated ferrite nanoparticles supercapacitor, a slower scan rate is an effective strategy. Regardless of the scanning rate used, the oxidation and reduction peaks almost always appeared at the same redox potentials. This could be attributed to the easy charge transfer across the material, high reversibility, and increased electrolyte diffusion rate within the nanostructure of the ferrite. As the scan rate increases from 5 to 200 mV/s,

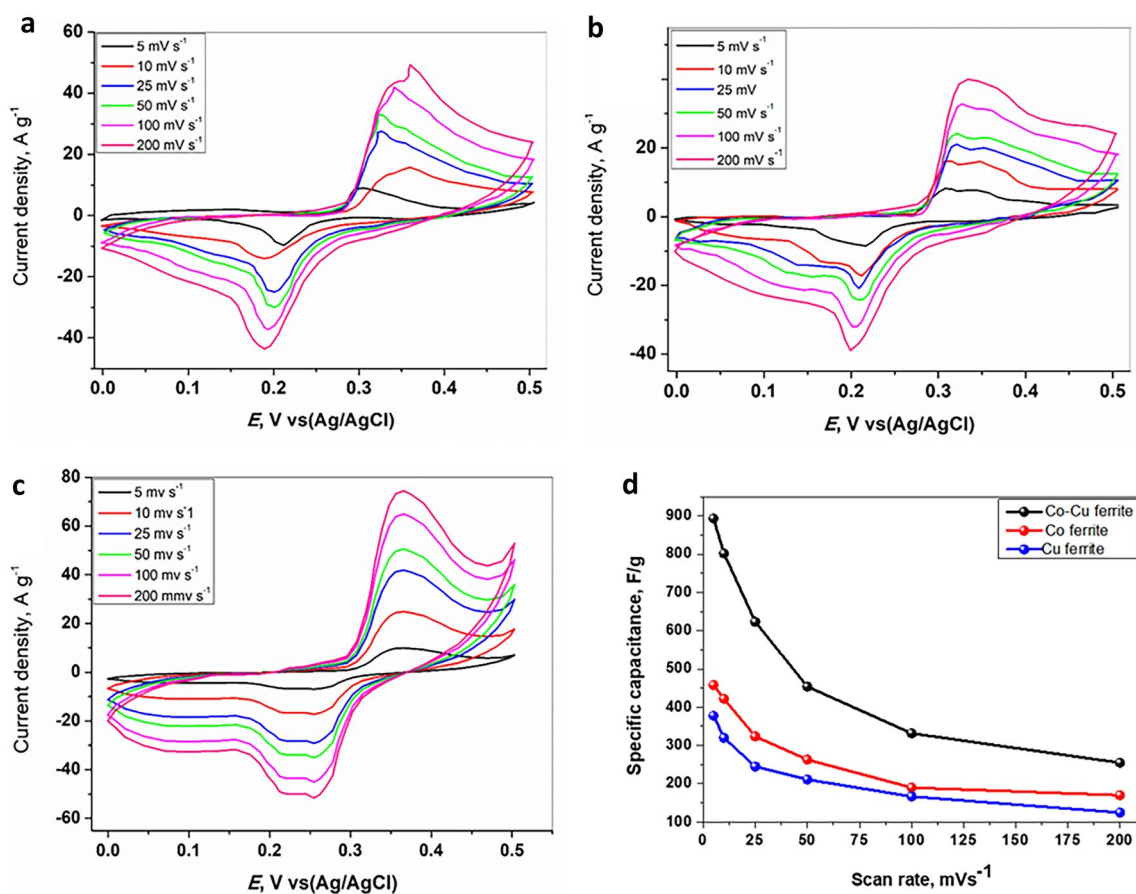


**Fig. 8** CV curves of ferrite nanoparticles. **a** Co ferrite, **b** Cu ferrite and **c** Co–Cu ferrite at different scan rates of 5, 10, 25, 50, 100 and 200 mV/s in 1 M KOH electrolyte. **d** Plot between specific capacitance and scan rate

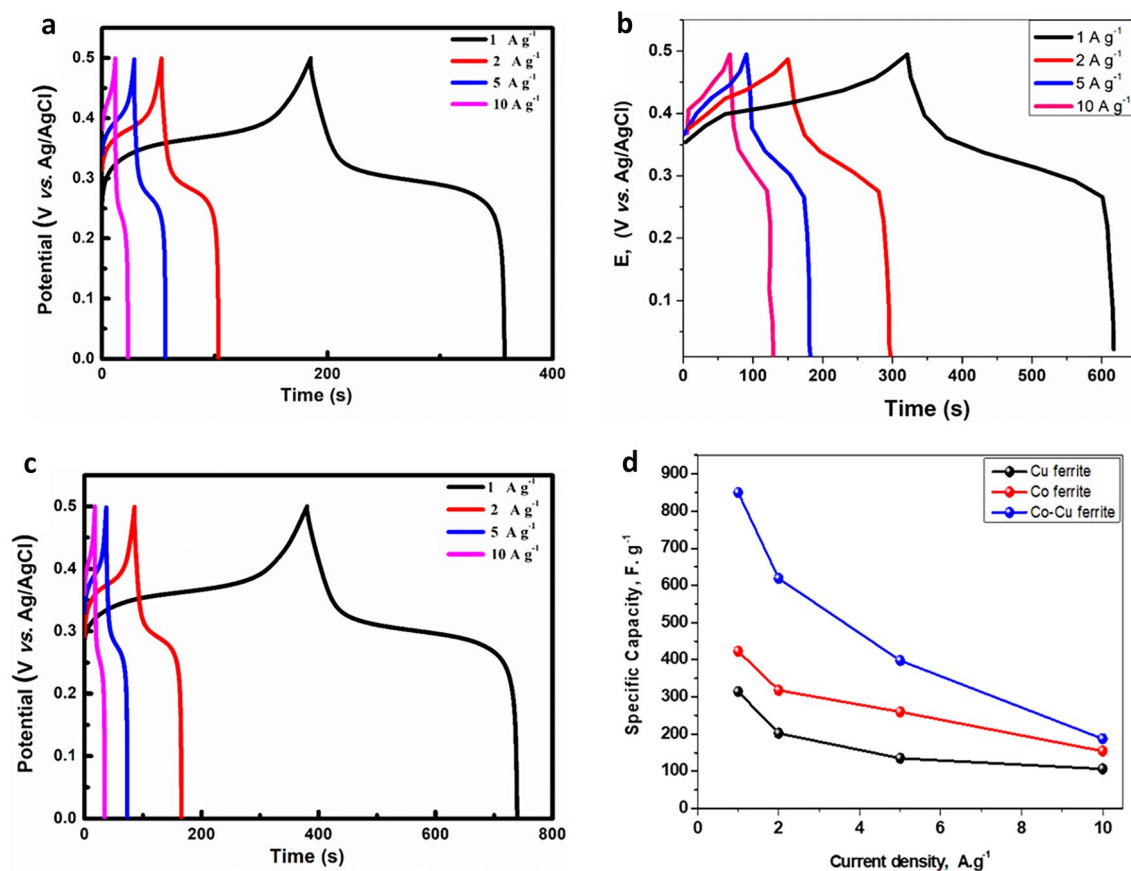


**Fig. 9** GCD curves of **a** Cu ferrite, **b** Co ferrite and **c** Co–Cu ferrite at different current densities of 1, 2, 5 and 10 A·g<sup>-1</sup> in 1 M KOH electrolyte, **d** plot of specific capacitance as a function of current density

the particular capacitance  $C_{sp}$  values decrease, as shown in Fig. 8d. The decrease in specific capacitance suggest that at high scan rates, the occurrence of inner active sites cannot completely sustain the redox transition, which could be due to the proton diffusion effect inside the electrode. On the other hand, when scanning at high rates, the internal diffusion resistance rises, resulting in an inevitable overpotential because electrolyte ions do not have enough time to reach the electrode surface [68]. With an increase in sweep rate, the area covered by CV loops for all working electrodes does not decrease, demonstrating great consistency in CV curves. The enhanced capacitive behavior and charge storage capacity of working electrodes are indicated by the excellent uniformity in the CV curve.

Galvanostatic charge/discharge (GCD) measurement is another accurate method for investigating the electrochemical performance of pseudo-supercapacitors [69]. The GCD curves for the investigated ferrite nanoparticles in 1 M KOH are shown in Fig. 9. Because of its pseudocapacitive nature, the investigated ferrite nanoparticle GCD curves deviate from linearity. With a declining current density, the investigated ferrite nanoparticles electrode

shows longer charging and discharging times, resulting in higher specific capacitance values (Fig. 9).  $C_{sp}$  decreases from 850 to 178 F/g, 423 to 154 F/g and 314 to 106 F/g for Co–Cu ferrite, Co ferrite and Cu ferrite, respectively, when the current density is increased from 1 to 10 A/g. The discharge time in Co–Cu ferrite nanoparticles GCD curves is significantly longer than in other materials indicating a much higher specific capacitance. The calculated specific capacitance of various samples at various current densities is shown in Fig. 9d. As the current density increases, the sample special capacitance decreases, as shown in the graph. Because of the diffusion effect of a proton inside the electrode, the occurrence of inner active sites cannot completely sustain the redox transition at high current density. At current densities of 1, 2, 5 and 10 A g<sup>-1</sup>, the Co–Cu ferrite has the highest unique capacitance values of 850, 619, 619 and 187 F g<sup>-1</sup>, respectively. As can be seen in Fig. 9d, it can be noted that the electrochemical performance of Co–Cu ferrite electrodes are significantly better than that of Co ferrite and Cu ferrite electrodes, which is superior to previously reported ferrites supercapacitor electrodes.

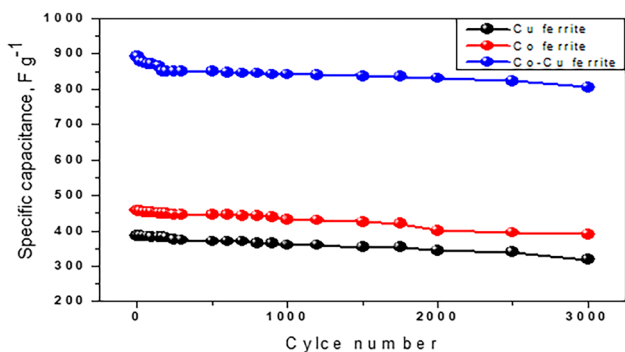


Fig. 10 Cycling stability curves of as-synthesized ferrite nanoparticles

### 4 Stability in cycling

Cycling stability (capacitance retention %) is another important factor in supercapacitor longevity. The capacitance retention (%) of the investigated ferrite nanoparticles was measured over 3000 GCD cycles at 1 A/g current density as shown in Fig. 10. After 3000 GCD cycles, the capacitance remains at 82.4, 85.15 and 90.14% for Cu ferrite, Co ferrite and Co–Cu ferrite demonstrating good long-term stability, and Co–Cu ferrite has higher stability than the other ferrite which may be ascribed to the effect of binary metals and small particle size.

Electrochemical impedance spectroscopy (EIS) is a useful technique and characterization tool for studying the electrode/electrolyte interface in supercapacitors [70]. The electrode internal resistance and electrode–electrolyte charge transfer resistance are shown in the EIS [71]. Figure 11 shows the EIS spectrum (Nyquist plot) of ferrite nanoparticles. In the high-frequency range, the plots of all materials show a semicircle, and in the low-frequency zone, a straight line. The charge-transfer resistance is related to the semicircle at high frequencies. The charge-transfer resistance increases with the diameter of the semicircle. The vertical line in the low-frequency region suggests that the electrolyte/electrode redox reactions were regulated by the mass transfer process, i.e., diffusion-controlled reactions. An equivalent circuit (EC) is given based on the EIS results. The solution resistance  $R_s$  is connected to the (CPE  $R_{ct}W$ ) time constant in the proposed EC model, which defines the depressed semicircle.  $C$  represents the double layer capacitance,  $R_{ct}$  represents the faradaic process-induced charge transfer resistance, and Warburg impedance ( $W$ ) represents the frequency-dependent electrolyte diffusion resistance. The fitted values of  $R_{ct}$  and  $R_s$  for all three samples are 4.9, 5.8, 9.4 and 0.30, 0.36, 0.25 for Co–Cu ferrite, Co ferrite and Cu ferrite, respectively, indicating that the charge transfer resistance and solution resistance of Co–Cu ferrite samples are higher than that of Co ferrites and Cu ferrite samples.

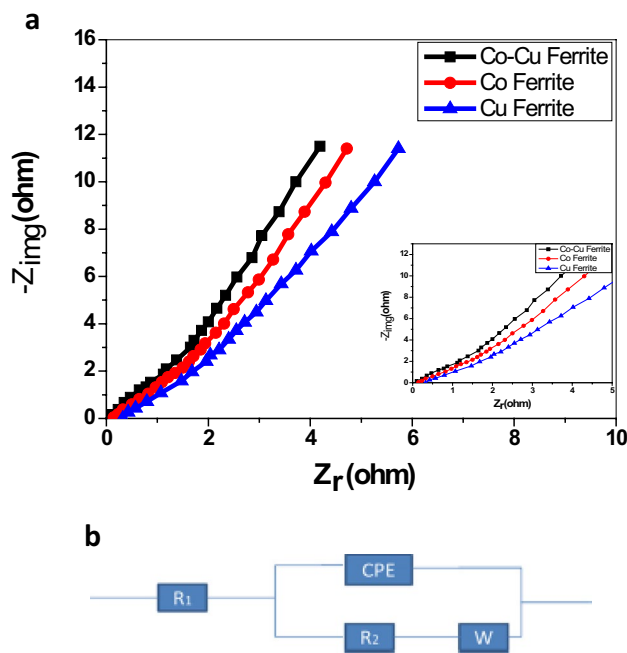


Fig. 11 a Nyquist plot of ferrite nanoparticles, b equivalent circuit

Furthermore, the low  $R_{ct}$  values imply a rapid kinetics on the electrode surface, implying that the phenomena are governed by diffusion, which is consistent with the cyclic voltammetry data. The fitted values of  $W_d$  of three samples are  $0.61 \Omega s^{-0.5}$ ,  $0.80 \Omega s^{-0.5}$ , and  $0.90 \Omega s^{-0.5}$ , indicating that the Co–Cu ferrite sample has a lower Warburg impedance than Co ferrites and Cu ferrite samples. This indicates that Co–Cu ferrite sample has higher ionic and electronic conductivity than the other samples.

### 5 Conclusion

Ferrite magnetic nanoparticles have been progressively synthesized using the citrate spontaneous combustion method. Microstructural investigation confirms the formation of the single-phase cubic spinel structure, and the morphological analyses from FESEM and HRTEM micrographs reveal the formation of nanosized particles. Surface area measurements reveal that these cobalt ferrite NPs have a mesoporous structure. The supercapacitive performances of ferrite nanoparticles were studied using cyclic voltammetry (CV), charge discharge, and electrochemical impedance spectroscopy (EIS) in 1 M KOH solution as the electrolyte. At a scan rate of  $5 \text{ mV s}^{-1}$ , the specific capacitance of ferrite nanoparticles was calculated to be 378, 458, and  $893 \text{ F g}^{-1}$ , respectively. When compared to other metal ferrite nanoparticles, Co–Cu ferrite had the highest specific capacitance. After 3000 cycles, the Co–Cu ferrite electrode has a 90% retention

retention. Co–Cu ferrite electrode is a promising candidate for suction due to its excellent properties.

**Acknowledgements** The authors thank the National Research Centre (NRC) for the technical and financial support.

**Author contributions** SAAK: conceptualization, formal analysis, writing—review and editing, project administration, funding acquisition, supervision, RR: formal analysis. MME-M: conceptualization, formal analysis.

**Funding** Open access funding provided by The Science, Technology & Innovation Funding Authority (STDF) in cooperation with The Egyptian Knowledge Bank (EKB).

**Availability of data and materials** All data and materials are available.

## Declarations

**Conflict of interest** The authors declare that they have no conflict of interest.

**Ethical approval** Not applicable.

**Consent to participate** The authors are constant to participate the article.

**Consent to publish** The authors constant to publish the article.

**Open Access** This article is licensed under a Creative Commons Attribution 4.0 International License, which permits use, sharing, adaptation, distribution and reproduction in any medium or format, as long as you give appropriate credit to the original author(s) and the source, provide a link to the Creative Commons licence, and indicate if changes were made. The images or other third party material in this article are included in the article's Creative Commons licence, unless indicated otherwise in a credit line to the material. If material is not included in the article's Creative Commons licence and your intended use is not permitted by statutory regulation or exceeds the permitted use, you will need to obtain permission directly from the copyright holder. To view a copy of this licence, visit <http://creativecommons.org/licenses/by/4.0/>.

## References

1. M. Hoel, S. Kverndokk, *Resour. Energy Econ.* **18**, 115–136 (1996)
2. S. Shafiee, E. Topal, *Energy Policy* **37**, 181–189 (2009)
3. D.E. Scaife, *Sol. Energy* **25**, 41–54 (1980)
4. Y. Shao, M.F. El-Kady, J. Sun, Y. Li, Q. Zhang, M. Zhu, H. Wang, B. Dunn, R.B. Kaner, *Chem. Rev.* **118**, 9233–9280 (2018)
5. J.S. Sagu, K.G.U. Wijayantha, A.A. Tahir, *Electrochim. Acta* **246**, 870–878 (2017)
6. S.S. Patil, D.P. Dubal, V.G. Deonikar, M.S. Tamboli, J.D. Ambekar, P. Gomez-Romero, S.S. Kolekar, B.B. Kale, D.R. Patil, *ACS Appl. Mater. Interfaces.* **8**, 31602–31610 (2016)
7. P. Simon, Y. Gogotsi, B. Dunn, *Science* **343**, 1210–1211 (2014)
8. F. Hekmat, H. Hosseini, S. Shahrokhian, H.E. Unalan, *Energy Storage Mater.* **25**, 621–635 (2020)
9. N. Choudhary, C. Li, J. Moore, N. Nagaiah, L. Zhai, Y. Jung, J. Thomas, *Adv. Mater.* **29**, 1605336 (2017)
10. L. Hao, X. Li, L. Zhi, *Adv. Mater.* **25**, 3899–3904 (2013)
11. Y. Shabangoli, M.S. Rahmanifar, M.F. El-Kady, A. Noori, M.F. Mousavi, R.B. Kaner, *Energy Storage Mater.* **11**, 282–293 (2018)
12. C.D. Lokhande, D.P. Dubal, O.S. Joo, *Curr. Appl. Phys.* **11**, 255–270 (2011)
13. C. Yuan, H.B. Wu, Y. Xie, X.W. Lou, *Angewandte Chemie – Int. Edition* **53**, 1488–1504 (2014)
14. M.A. Mousa, M. Khairy, M. Shehab, J. Solid State Electrochem. **21**, 995–1005 (2017)
15. K.K. Kefeni, T.A.M. Msagati, B.B. Mamba, *Mater. Sci. Eng. B: Solid-State Mater. Adv. Technol.* **215**, 37–55 (2017)
16. Y.L. Pang, S. Lim, H.C. Ong, W.T. Chong, *Ceram. Int.* **42**, 9–34 (2016)
17. M. Khairy, M. Mousa, *Int. J. Mater. Chem.* **2**, 197–204 (2012)
18. J. Ding, P.G. McCormick, R. Street, *J. Magn. Magn. Mater.* **171**, 309–314 (1997)
19. D. Chen, D.Y. Li, Y.Z. Zhang, Z.T. Kang, *Ultrason. Sonochem.* **20**, 1337–1340 (2013)
20. R. Singh, M. Kumar, L. Tashi, H. Khajuria, H.N. Sheikh, *Nanochem. Res.* **3**, 149–159 (2018)
21. P. Guo, G. Zhang, J. Yu, H. Li, X.S. Zhao, *Colloids Surf. A* **395**, 168–174 (2012)
22. V. Blanco-Gutierrez, R. Saez-Puche, M.J. Torralvo-Fernandez, *J. Mater. Chem.* **22**, 2992–3003 (2012)
23. J. Wang, Q. Chen, B. Hou, Z. Peng, *Eur. J. Inorg. Chem.* **2004**, 1165–1168 (2004)
24. N. Bao, L. Shen, Y.H.A. Wang, J. Ma, D. Mazumdar, A. Gupta, *J. Am. Chem. Soc.* **131**, 12900–12901 (2009)
25. S. Zhang, D. Dong, Y. Sui, Z. Liu, H. Wang, Z. Qian, W. Su, *J. Alloy. Compd.* **415**, 257–260 (2006)
26. S.D. Sartale, C.D. Lokhande, *J. Electroceram.* **15**, 35–44 (2005)
27. Y. Xu, J. Wei, J. Yao, J. Fu, D. Xue, *Mater. Lett.* **62**, 1403–1405 (2008)
28. S.-L. Kuo, N.-L. Wu, *Electrochem. Solid-State Lett.* **8**, A495 (2005)
29. G. Nabi, W. Raza, M.A. Kamran, T. Alharbi, M. Rafique, M.B. Tahir, S. Hussain, N.R. Khalid, Q. ul-Aain, N. Malik, R.S. Ahmed, C.B. Cao, *J. Energy Storage* **29**, 101452 (2020)
30. B. Bhujun, M.T.T. Tan, A.S. Shanmugam, *Ceram. Int.* **42**, 6457–6466 (2016)
31. W. Wang, Q. Hao, W. Lei, X. Xia, X. Wang, *J. Power Sources* **269**, 250–259 (2014)
32. A.Y. Faid, H. Ismail, *Mater. Today Energy* **13**, 285–292 (2019)
33. V.S. Kumbhar, A.D. Jagadale, N.M. Shinde, C.D. Lokhande, *Appl. Surf. Sci.* **259**, 39–43 (2012)
34. B.J. Rani, G. Ravi, R. Yuvakkumar, V. Ganesh, S. Ravichandran, M. Thambidurai, A.P. Rajalakshmi, A. Sakunthala, *Appl. Phys. A* **124**, 511 (2018)
35. F.M. Ismail, M. Ramadan, A.M. Abdellah, I. Ismail, N.K. Allam, *J. Electroanal. Chem.* **817**, 111–117 (2018)
36. S. Pawar, S. Patil, M. Chithra, S.C. Sahoo, P. Patil, *Cobalt Ferrite Nanoparticles for Supercapacitor Application. AIP Conference Proceedings*, AIP Publishing LLC, 2020, p. 030162.
37. D. Deng, H. Pang, J. Du, J. Deng, S. Li, J. Chen, J. Zhang, *Cryst. Res. Technol.* **47**, 1032–1038 (2012)
38. M. Hasanin, S.A. Al Kiey, *Biomass Convers. Biorefin.* (2021).
39. S.A. Al Kiey, M.S. Hasanin, S. Dacrory, *J. Mol. Liq.* **338**, 116604 (2021)
40. A.M. Fahim, R.E. Abouzeid, S.A. Al Kiey, S. Dacrory, *J. Mol. Struct.* **1247**, 131390 (2022)
41. R.M. Abdelhameed, S.A. Al Kiey, A.R. Wassel, M. El-Shahat, *New J. Chem.* (2021)
42. S.A. Al Kiey, M.S. Hasanin, *Environ. Sci. Pollut. Res.* **1–13** (2021)
43. H.N. Abdelhamid, S.A. Al Kiey, W. Sharmoukh, *Appl. Organometall. Chem.* **36**, e6486 (2022)

44. C. BD, Elements of X-ray Diffraction., Boston: Addison-Wesley, 1978.
45. C.N.M. Uryanarayana, *X-ray Diffraction: A Practical Approach* (Plenum Publishing Corporation, New York, 1998)
46. R. Waldron, Phys. Rev. **99**, 1727 (1955)
47. N. Singh, K. Rachna, Environmental nanotechnology. Monitor. Manag. **14**, 100301 (2020)
48. M.M. El-Masry, R. Ramadan, M. Ahmed, Results Mater. **8**, 100160 (2020)
49. K.C.B. Naidu, M. Wuppulluri, IEEE Trans. Magn. **54**, 1–8 (2018)
50. J. Baraliya, H. Joshi, Vib. Spectrosc. **74**, 75–80 (2014)
51. P. Chandramohan, M. Srinivasan, S. Velmurugan, S. Narasimhan, J. Solid State Chem. **184**, 89–96 (2011)
52. L.V. Gasparov, D.B. Tanner, D.B. Romero, H. Berger, G. Margaritondo, L. Forró, Phys. Rev. B – Condens. Matter Mater. Phys. **62**, 7939–7944 (2000)
53. T. Yu, Z. Shen, Y. Shi, J. Ding, J. Phys.: Condens. Matter **14**, L613 (2002)
54. S.G. Kakade, Y.-R. Ma, R.S. Devan, Y.D. Kolekar, C.V. Ramana, J. Phys. Chem. C **120**, 5682–5693 (2016)
55. C. Koops, Phys. Rev. **83**, 121 (1951)
56. K. Wagner, Ann. Phys **40**, 817–855 (1913)
57. R. Kambale, P. Shaikh, C. Bhosale, K. Rajpure, Y. Kolekar, Smart Mater. Struct. **18**, 085014 (2009)
58. R.S. Yadav, I. Kuřitka, J. Vilcakova, J. Havlica, J. Masilko, L. Kalina, J. Tkacz, J. Švec, V. Enev, M. Hajdúchová, Adv. Nat. Sci.: Nanosci. Nanotechnol. **8**, 045002 (2017)
59. N. Sivakumar, A. Narayanasamy, B. Jeyadevan, R.J. Joseyphus, C. Venkateswaran, J. Phys. D Appl. Phys. **41**, 245001 (2008)
60. Y. Kolekar, L. Sanchez, C. Ramana, J. Appl. Phys. **115**, 144106 (2014)
61. J. Balavijayalakshmi, N. Suriyanarayanan, R. Jayaprakash, Mater. Lett. **81**, 52–54 (2012)
62. C.L. Louis-Philippe Carignana, A. Ouimet, M. Ciureanu, A. Yelon, and D. Ménard, J. Appl. Phys. **102** (2007)
63. K.V.R. Tholkappiyan, Appl. Surf. Sci. **351**, 1016–1024 (2015)
64. J.J.V. J. Arul Mary, M. Bououdina, L. John Kennedy, J.H. Dai, Y. Song, Physica E: Low-Dimension Syst. Nanostruct. **66**, 209–220 (2015)
65. Y. Gogotsi, R.M. Penner, Energy storage in nanomaterials—capacitive, pseudocapacitive, or battery-like?, ACS Publications, 2018.
66. L. Sun, Y. Zhang, Y. Zhang, H. Si, W. Qin, Y. Zhang, Chem. Commun. **54**, 10172–10175 (2018)
67. M. Toupin, T. Brousse, D. Bélanger, Chem. Mater. **16**, 3184–3190 (2004)
68. T. Cottineau, M. Toupin, T. Delahaye, T. Brousse, D. Bélanger, Appl. Phys. A **82**, 599–606 (2006)
69. L. Zhou, C. Li, X. Liu, Y. Zhu, Y. Wu, T. van Ree, Metal Oxides in Energy Technologies, Elsevier, pp. 169–203 (2018)
70. A.D. Jagadale, V.S. Kumbhar, D.S. Dhawale, C.D. Lokhande, Electrochim. Acta **98**, 32–38 (2013)
71. A. Rai, A.L. Sharma, A.K. Thakur, Solid State Ionics **262**, 230–233 (2014)

**Publisher's Note** Springer Nature remains neutral with regard to jurisdictional claims in published maps and institutional affiliations.